Environmental Functional Materials 1 (2022) 196–203

Contents lists available at ScienceDirect

Environmental Functional Materials

journal homepage: www.keaipublishing.com/en/journals/environmental-functional-materials

Development of an innovative MnO_2 nanorod for efficient solar vapor generator

Casey Onggowarsito, An Feng, Shudi Mao, Stella Zhang, Idris Ibrahim, Leonard Tijing, Qiang Fu *, Huu Hao Ngo

Centre for Technology in Water and Wastewater, School of Civil and Environmental Engineering, University of Technology Sydney, Ultimo, 2007, Australia

GRAPHICAL ABSTRACT

Hydrogel-based solar vapor generator containing high thermal generating photo-thermal material for efficient desalination process via sunlight to produce freshwater.

ARTICLE INFO

Keywords:
Solar vapor generation
Hydrogel network
Photo-thermal material
Broad light absorption
High thermal generation
Low evaporation enthalpy
Desalination

ABSTRACT

Finding an efficient water harvesting technique is currently highly sought-after due to the rise of water demand. Solar vapor generators (SVGs) have recently shown promising results to be used as a cleaner alternative water harvesting system for desalination application. However, recent SVGs using semiconductor as photo-thermal materials (PTMs) still suffer from a low average water evaporation performance. This study aims to develop a novel high-water generating hydrogel-based SVG consisting of cross-linked polyvinyl alcohol (PVA) matrix and designed MnO_2 nanorods as solar-to-heat converter. Results indicated that the resultant hydrogel material exhibited a maximum water evaporation rate of 2.8 kg/(m^2·h) under 1 sun. Furthermore, the PVA/MnO_2 hydrogel demonstrated salt resistant and filtration capability for desalination application with a consistent evaporation rate of 2.8 kg/(m^2·h) and >99.8% reduction of sodium ion concentration. In short, this study opens up a new pathway for the development of high performance SVG system for desalination applications.

1. Introduction

Over the past 100 years, water demand has surged by a factor of six and has been continuously increasing at a rate of 1% per annum due to factors such as industrial, domestic, and agriculture water usage [1,2]. Agriculture production has taken 70% of the global water demand [3–5]

* Corresponding author. Centre for Technology in Water and Wastewater, School of Civil and Environmental Engineering, University of Technology Sydney, Ultimo, 2007, Australia.
E-mail address: Qiang.Fu@uts.edu.au (Q. Fu).

https://doi.org/10.1016/j.efmat.2022.08.001
Received 18 July 2022; Received in revised form 10 August 2022; Accepted 17 August 2022

and the water demand for energy and manufacturing production will increase to 85% and 400% respectively [1,2,6]. Furthermore, with the gradual increase of population however, domestic water usage is predicted to increase 130% by 2050 [1,7–11]. Besides the increasing water demand, wastewater containing detrimental elements such as microplastics, heavy metals, organics, nitrogen and phosphorus fertilizer pollutants may further degrade our freshwater resource [2,12–15]. Currently, used water production system rely on desalination technologies such as multi-effect distillation (thermal desalination) and electrodialysis desalination (membrane desalination) for freshwater production [16,17]. However, these systems tend to leave a large environmental footprint as well as being cost-ineffective due to labor, operational, and maintenance cost [18–20].

As a replacement, recent strategy of interfacial solar vapor generation (SVG) has caught increasing attentions due to its practicality and promising water generating performance [21–23]. Similar to desalination techniques, interfacial SVG involves generating clean water through water evaporation from internally heating the water source caused by photothermal materials (PTMs) exposure to sunlight [24]. An example of interfacial SVG can been seen in luffa-inspired PC@PDA-C aerogel developed by Liu et al. [25]. This nanofiber-based aerogel was able to produce a high evaporation rate of 2.13 kg/(m^2·h) with 94.5% solar-vapor conversion efficiency under 1 sun, which is the result of the enhancing photothermal effect of PTMs. Li et al. [26] developed an aero-cryogel monolith SVG consisted of polyaniline and carboxymethyl cellulose, achieving 2.16 kg/(m^2·h) water evaporation with 93.6% efficiency under 1 sun. The authors highlighted that the hydrophilic polymer allows the gel to have lower evaporation enthalpy as large amount of weakly bonded water molecules were found.

Carbon-based materials, noble plasmonic nanoparticles, conjugated polymers, and inorganic semiconductors are known to contain broad light absorption property for an optimum solar-thermal energy conversion [22,24,27–29]. Among them, one-dimensional (1D) [30–32] or and two-dimensional (2D) carbon materials (i.e., carbon nanotubes, reduced graphene oxides, etc.) [33–35] have been widely employed as PTMs in hydrogel-based SVGs due to their wide availability, high solar-to-heat conversion and high heat conductivity. However, the hydrophobic surface of these PTMs results in relatively high evaporation enthalpy and poor water transport within the composite hydrogels, which in turn limits the evaporation performance. On the other hand, the inorganic semiconductors used in SVGs are mostly 3D spherical particles with hydrophilic surfaces. We thus saw this as an opportunity to develop novel 1D inorganic semiconductors to simultaneously achieve high solar-to-heat conversion, high heat conductivity, lower evaporation enthalpy and high water transport.

In this study, we developed a low-cost and high performing hydrogel-based SVG consisting of 1D nanorods and 3D particles metal oxide (MnO_2) as PTM, as well as hydrophilic polyvinyl alcohol (PVA) matrix. The prepared MnO_2 nanorods and particles displayed high aspect ratio, high water affinity, high surface area and high solar-thermal conversion efficiency. However, it is expected that PVA/1D-MnO_2 hydrogel would outperform its PVA/3D-MnO_2 counterpart due to possessing lower evaporation enthalpy and faster water transport. As a result, the developed PVA/1D-MnO_2 SVG system managed to produce a high-water evaporation rate of 2.8 kg/(m^2·h) with a very high efficiency under 1 sun. Furthermore, we demonstrated the SVG system has high salt resistance and stable performance when exposed to seawater, indicating that it has the potential to be a greener alternative to our current desalination systems.

2. Experimental

2.1. Materials

All reagents including polyvinyl alcohol (PVA, Mw: 89–98 kDa), glutaraldehyde (GA, 25% aqueous solution), potassium permanganate ($KMnO_4$,>99%), manganese(II) sulfate monohydrate ($MnSO_4·H_2O$, >98%) were purchased from Sigma-Aldrich and used without any further purification. Both MnO_2 tunnel/birnessite structures were prepared according to the literature [36].

2.2. Preparation of inorganic MnO_2 particles and nanorods

MnO_2 was produced via redox reaction of $KMnO_4$ and $MnSO_4·H_2O$. In a typical reaction, 1 g $KMnO_4$ was dissolved in 75 mL of deionized water. 0.1 g and 1 g of $MnSO_4·H_2O$ was added to $KMnO_4$ solution to produce MnO_2 end product with birnessite (MnO_2 0.1:1) and tunnel (MnO_2 1:1) structure respectively. Both mixture solutions were heated via hydrothermal reaction overnight at 200 °C producing precipitates to be collected, dried, and washed three times with deionized water. Both precipitates were then calcined at 300 °C for 3 h with a heating rate of 10°/min under nitrogen gas protection with a flow rate of approximately 10 mL/s.

2.3. Preparation of PVA/MnO_2 hydrogel SVG

PVA solution (10 wt%) was prepared by dissolving PVA (Mw: 89–98 kDa) with deionized water under 80 °C for approximately 5 h. Both MnO_2 structures at different weight percentages (5%, 10%, and 15%) were then mixed with the prepared 2 mL PVA solution producing hydrogel solutions. 50 μL glutaraldehyde (25 wt%) followed by 100 μL HCl (1 M) were added into the mixtures before then freezing it overnight for gelation process to take place. Frozen hydrogel samples were than thawed at room temperature and integrated on a polystyrene foam for water evaporation performance testing to take place.

2.4. Characterization

Scanning electron microscope (SEM) imaging Zeiss EVO LS15 SEM system was used to show MnO_2 and PVA/MnO_2 hydrogels microstructure. PVA/MnO_2 hydrogels were frozen dried prior to SEM imaging. Fourier-Transform infrared spectroscopy (FTIR) spectra of PVA, MnO_2, and PVA/MnO_2 hydrogels were taken by SHIMADZU MIRacle 10 single reflection ATR accessory. Renishaw Raman spectroscopy was used to calculate the intermediate water (IW) to free water (FW) ratio. Absorption spectra of PVA/MnO_2 hydrogels were taken in the range of 200–2500 nm by ultraviolet–visible–near infrared (UV-VIS-NIR) Cary 7000 Universal Measurement Spectrophotometer. MnO_2 and PVA/MnO_2 hydrogels surface temperature were measured and taken by Fluke PTi120 thermal imaging camera. PVA and PVA/MnO_2 hydrogels vaporization enthalpy were measured with Q600 SDT Thermal Analyzer (DSC-TGA). Desalinated water salinity concentration was analyzed with Agilent 7900 ICP-MS.

2.5. Solar vapor generation experiment

Water evaporation testing were conducted on an inhouse built cabinet box consisting of a solar light simulator (NBeT HSX-F3000 xenon light source) calibrated to 1 sun irradiation (≤1 kW/m^2), analytical balance (OHAUS Pioneer IC-PX 124), and a thermal camera (Fluke PTi120). Solar light simulator will be switched on in advance approximately for 1 h, allowing the ambient conditions to hit equilibrium before starting the experiment. Hydrogels are placed on top of a water source (DI water/seawater) to test its water evaporation rate under light exposure (light evaporation) and without light exposure (dark evaporation) to take account natural evaporation. The water mass loss for light and dark evaporation ($\dot{m}_{light}$ and $\dot{m}_{dark}$) will be recorded for every 4 min in an hour interval.

3. Results and discussion

3.1. The preparation of 1D MnO_2 nanorods

1D inorganic MnO_2 semiconductor was synthesized, investigated, and compared to its 3D counterpart. The morphology of MnO_2 PTM can tuned by adjusting $MnSO_4{\cdot}H_2O$:$KMnO_4$ weight ratio of 0.1:1 and 1:1, where in this study they are designated as 3D MnO_2 (0.1:1) and 1D MnO_2 (1:1), respectively. Based on the SEM images shown in Fig. 1a and b, the spherical 3D MnO_2 particles have an average diameter of ~1.15 μm. On the contrary, the 1D MnO_2 rod have an average dimension of ~12 μm in length and ~50 nm in width (Fig. 1e and f). The wide exposed surface areas of both structures allow a high amount of light absorption (from 300 to 2500 nm) allowing for high thermal generation as shown in Fig. 1c–d and 1g-1h. Specifically, after 60 min irradiation, the 3D MnO_2 particles and 1D MnO_2 nanorods displayed an elevated temperature of 74.7 °C and 83.9 °C respectively, suggesting their excellent ability of solar-to-heat conversion.

3.2. The preparation of PVA/MnO_2 hydrogel SVG

With the 1D PTM in hand, we then constructed the hydrogel SVG. A typical synthesis of PVA/MnO_2 hydrogel was illustrated in Scheme 1. Both MnO_2 PTMs were randomly dispersed and mixed with the prepared 10 wt% PVA stock solution. The PVA/MnO_2 mixtures were then cross-linked by introducing glutaraldehyde and HCl (1 M). After standing for 30 min, the mixtures were placed in a freezer (−20 °C) overnight. The frozen gels were then thawed under room temperature for ~30 min before undergoing any water evaporation testing or characterization. In this study, six different types of gels were prepared with varying 1D or 3D MnO_2 PTMs loading (i.e., 5%, 10%, and 15%) for performance comparison and optimization purposes. The resultant PVA/MnO_2 hydrogels are designated as PVA/1D-MnO_2(x) or PVA/3D-MnO_2(x), where x is equal to 5, 10, 15%, respectively.

The prepared hydrogels were freeze dried before conducting SEM analysis. As shown in Fig. 2, both PVA/1D-MnO_2 and PVA/3D-MnO_2 hydrogels exhibit relatively high surface roughness (Fig. 2a and c) which minimizes light reflection, allowing the gels to have better light harvesting ability [37]. Furthermore, both gels contain continuous vertically aligned and random sized porous microstructure labelled in Fig. 2b and d, which helps to provide water transport/absorption [28,38,39].

We then characterized the PVA/MnO_2 hydrogel chemical compositions by FTIR spectrometer. As shown in Fig. 3a, both hydrogels exhibit characteristic peaks of PVA and MnO_2. The presence of MnO_2 is featured through the Mn–O stretching vibration at peaks between 400 and 650 cm^{-1} [40,41]. Moreover, the C–O and C═O stretching of PVA and the remaining acetate groups of glutaraldehyde at 1112 and 1650 cm^{-1} were observed. The C–H stretching of alkyl groups at 2840 cm^{-1}, and broad OH stretch at 3300 cm^{-1} emphasize PVA hydrophilic groups for water absorption [42,43]. The light harvesting ability of PVA/MnO_2 hydrogels can be demonstrated based on their light absorption capability. As shown in Fig. 3b, both PVA/3D-MnO_2 and PVA/1D-MnO_2 hydrogels display broad light absorption range from 300 to 2500 nm relative to pure PVA hydrogel. Due to this, PVA/MnO_2 hydrogels managed to produce fast solar-to-heat response rate as shown in Fig. 3c. In less than 20 min, all the PVA/MnO_2 hydrogels were able to reach its plateau surface temperature and continually to increase to its maximum temperature ranging between 35 and 37 °C.

Water transport rate (V) (Eq. (2)) of PVA/MnO_2 hydrogels were investigated through determining its water content (Q) (Eq. (1)), half-saturated time (t), and state (0.5 Q_s). PVA/MnO_2 hydrogels were freeze dried previous to this testing in order to obtain its dry state weight (W_{dry}). The frozen dried gels were then saturated and weighted, obtaining its swollen state (W).

$$Q = W / W_{dry} \tag{1}$$

$$V = 0.5\, Q_s / t \tag{2}$$

The result shows that PVA/MnO_2 saturated water content (Q_s) is dependable on MnO_2 loading contents and morphology. As shown in Fig. 3d, an increase of MnO_2 weight percentage causes Q_s of PVA/1D-MnO_2 to increase from 2.88, 3.49, and 4.93 g/g. However, in the series of PVA/3D-MnO_2 hydrogels, we observed a decrease in Q_s relative to the increase of MnO_2 weight percentage. This demonstrates that the

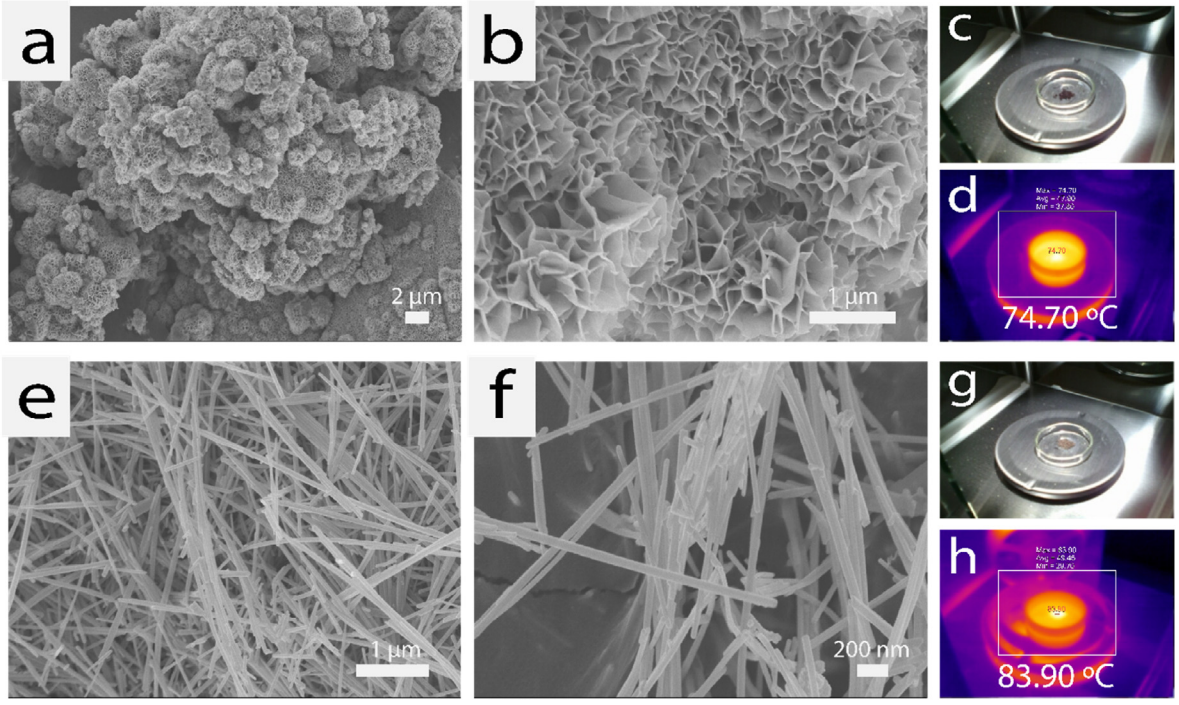

Fig. 1. SEM images of (a–b) 3D MnO_2 particles and (e–f) 1D MnO_2 nanorods. Visual and thermal images of 3D MnO_2 particles (c–d) and 1D MnO_2 nanorods (g–h).

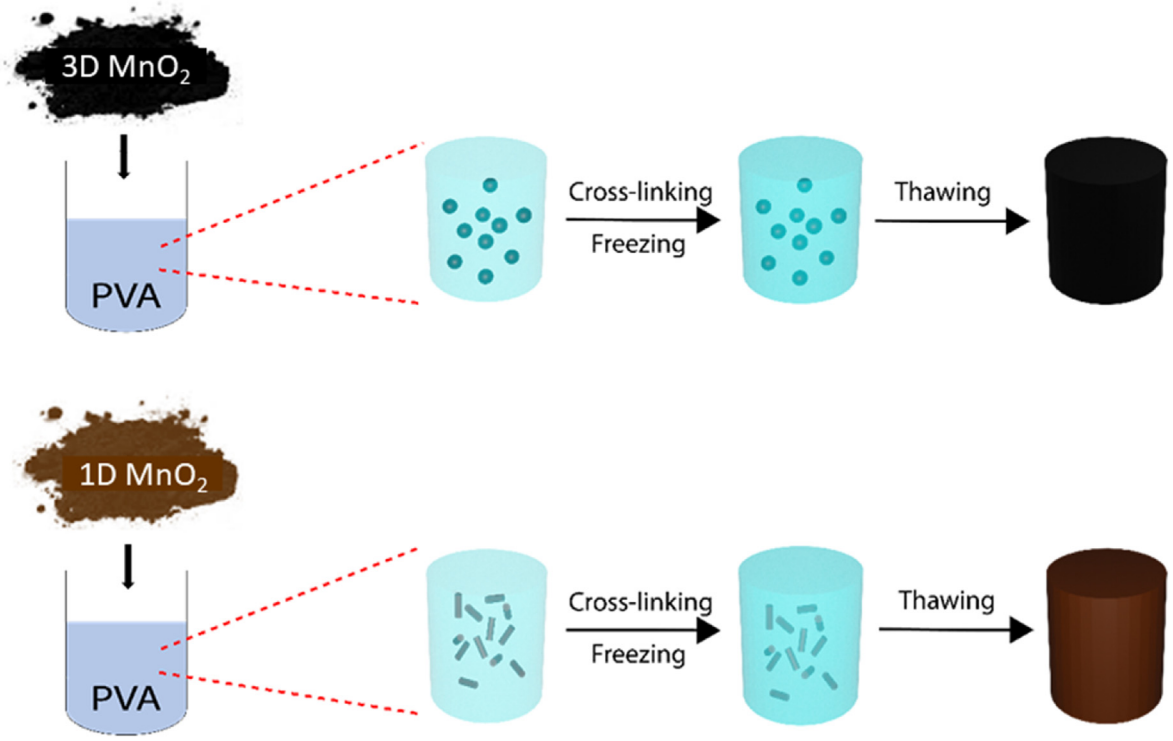

Scheme 1. Schematic illustration of PVA/MnO_2 hydrogel SVGs.

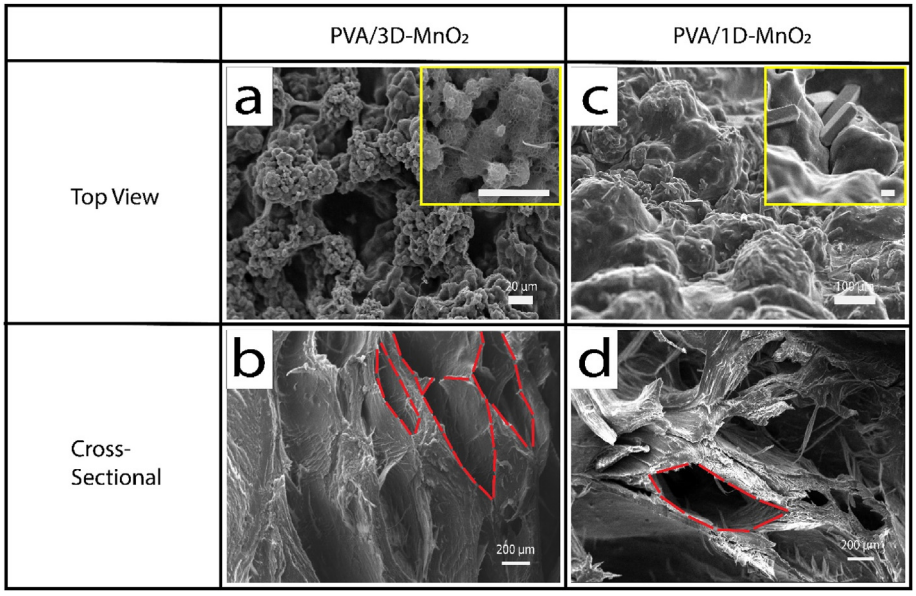

Fig. 2. (a, c) Surface structure and (b, d) cross-sectional SEM images of (a, b) PVA/3D-MnO_2 and (c, d) PVA/1D-MnO_2 hydrogels. The scale bars represent 10 μm in the inserts.

incorporation of MnO_2 nanorods can further enhance the water transport within the hydrogels, which may be attributed to their fiber-like morphology which create additional water transport pathways along the MnO_2 hydrophilic surface [44–46].

Besides Q_s, the half-swollen time of the hydrogels are also needed to be considered to determine water transport efficiency since the hydrogels will mostly be at a near fully saturated state due to constant sunlight and water source exposure. From Fig. 4a and b, both hydrogels obtained an optimum half-swollen time at 10 wt% MnO_2. Moreover, PVA/1D-MnO_2 hydrogels display a faster half-swollen time compared to PVA/3D-MnO_2 counterparts.

3.3. Solar vapor generation performance

In order to measure and compare the SVG performance of each system, at least three samples for each hydrogel with specific exposed surface area were placed on top of a water source and exposed to ~1 sun irradiation (Fig. 5a). SVG measurements were determined by the amount of water evaporation produced by each hydrogel. The average mass loss rates were shown in Fig. 5b. In short, the PVA/MnO_2 hydrogels manage

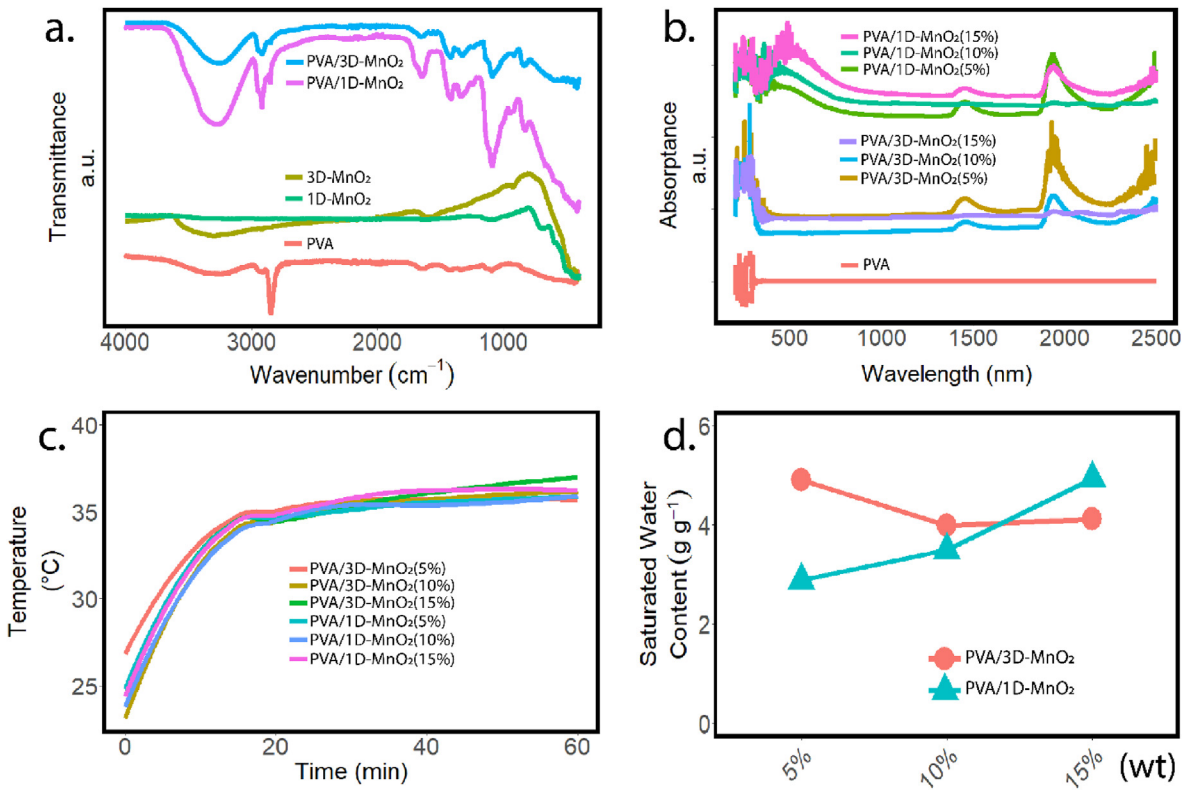

Fig. 3. (a) FTIR spectra of PVA, MnO_2, and PVA/MnO_2 hydrogel. (b) UV-VIS-NIR spectra of PVA and PVA/MnO_2 hydrogels. (c) PVA/MnO_2 hydrogels surface temperature throughout 1 h water evaporation testing. (d) Saturated water content comparison between PVA/3D-MnO_2 and PVA/1D-MnO_2.

to generate high-water evaporation rate compared to bulk water and pure PVA hydrogel. This can be attributed to the hydrogels' high surface temperature and low evaporation enthalpy (Fig. S3) due to the incorporation of PTMs and the presence of high intermediate water ratio (Figure S2.2), respectively. The PVA/1D-MnO_2(10%) was able to produce the highest net water evaporation rate of 2.8 kg/(m^2·h), compared to other PVA/MnO_2 hydrogels. Of particular note, in comparison to bulk water and PVA hydrogel net evaporation, PVA/1D-MnO_2(10%) generated 5.2 and 3.2 times higher respectively. Interestingly, both PVA/3D-MnO_2 and PVA/1D-MnO_2 hydrogels water evaporation rate is optimized at 10 wt% MnO_2 loading, where PVA/3D-MnO_2(10%) generated net evaporation rate of 2.6 kg/(m^2·h) as shown in Fig. 5c and d.

Furthermore, the solar-thermal conversion efficiency can be evaluated using Eq. (3):

$$\eta = \frac{\dot{m}(C_p \Delta T + \Delta H)}{c_{opt} I A \Delta t} \tag{3}$$

where $\dot{m}$ is the change of water mass from water evaporation, C_p is the specific heat capacity of water (4.18 J/(g·K)), ΔT is the temperature difference between vapor and ambient, ΔH is the vaporization enthalpy at the evaporation point, c_{opt} is the optical concentration, I is the solar irradiation (1 kW/m^2), A is the material's exposed surface area, and Δt is the exposure time [47]. As seen from Eq. (3), the energy conversion efficiency is highly dependent on the value of ΔH, which commonly can be determined by two methods [39,48]. In this study, we determined the ΔH s by DSC-TGA measurements (Fig. S2, details are available in Supporting Information). The PVA/3D-MnO_2 hydrogels managed to generate high evaporation performance and energy conversion efficiency with an increase of 3D MnO_2 loading percentage (Fig. 5c). At 10 and 15 wt%, PVA/3D-MnO_2 were able to have *ca.* 2.6 kg/(m^2·h), and 96% and 99% efficiency, respectively. PVA/1D-MnO_2 however showed an optimum efficiency at 10 wt% 1D MnO_2 loading. Specifically, the PVA/1D-MnO_2 (10%) displays a higher evaporation rate of 2.8 kg/(m^2·h) with a ΔH of 1411.8 kJ/kg and a conversion efficiency of 113%. In this study, conversion efficiency was calculated by considering the ΔH obtained by DSC-TGA and the real-time surface temperature of the hydrogel (Table S1, Supplementary Material). The excess efficiency may indicate that these hydrogels experienced energy/heat transfer from environment

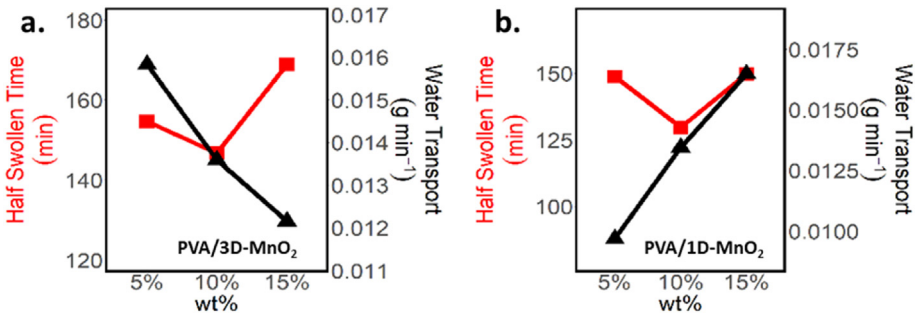

Fig. 4. Half-swollen time and water transport comparison between (a) PVA/3D-MnO_2 and (b) PVA/1D-MnO_2.

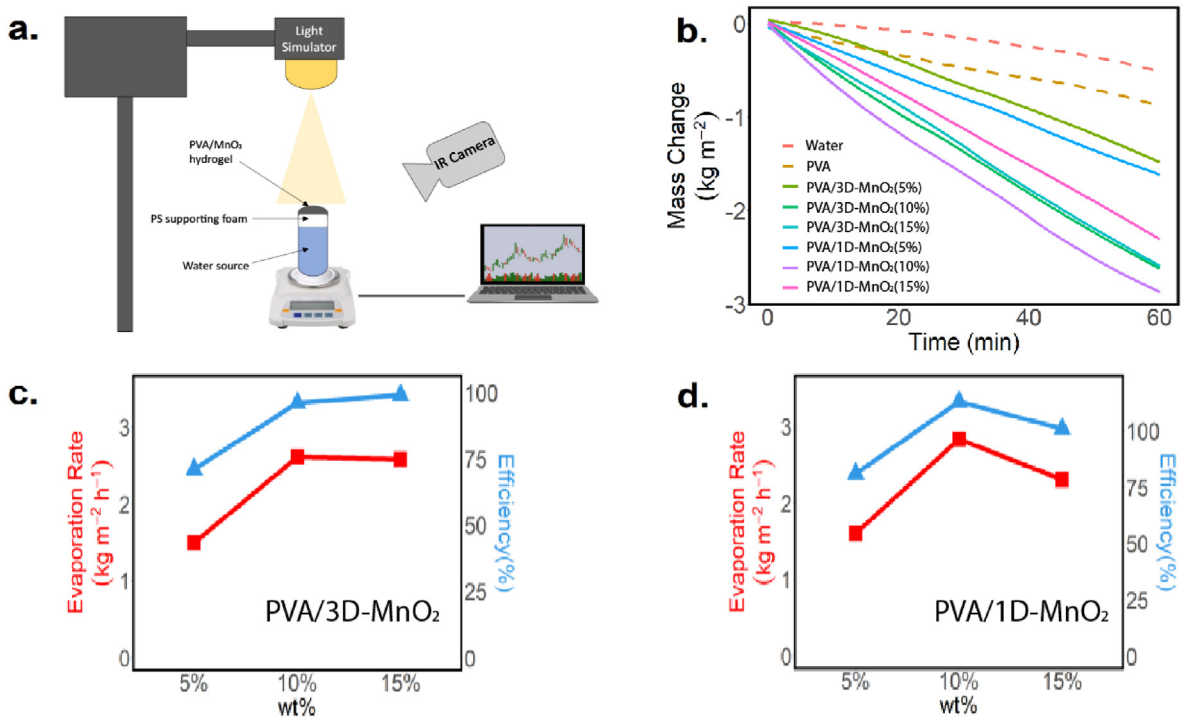

Fig. 5. (a) SVG set up. (b) Water mass loss rate between bulk water, PVA, and PVA/MnO_2 hydrogels. Evaporation rate and efficiency comparison between (c) PVA/3D-MnO_2 and (d) PVA/1D-MnO_2.

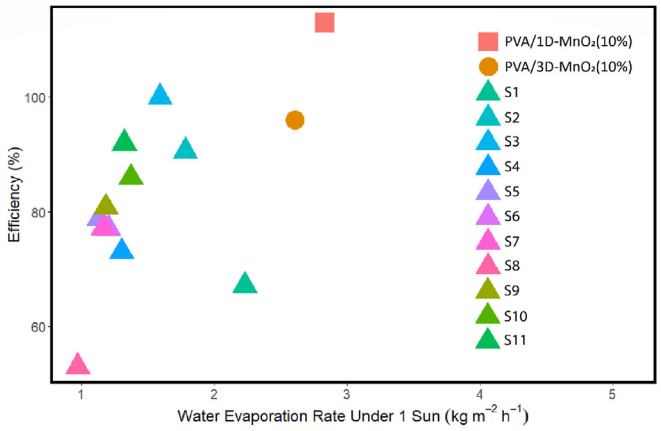

Fig. 6. The evaporation rate vs. energy conversion efficiency of the hydrogel-based SVGs using semiconductors. The details are listed in Table S2 (Supporting Material).

to the gels due to a temperature difference in the sealed system as experienced by Li et al. [49].

We further compared the performance of the PVA/1D-MnO_2(10%) with other SVGs using semiconductors as PTMs and the results are shown in Fig. 6. As seen, PVA/1D-MnO_2 and PVA/3D-MnO_2 were able to outproduce other semiconductor SVGs in water evaporation performance as well as conversion efficiency. This can be due to the low evaporation enthalpy that is produced by the PVA/MnO_2 matrix. For example, Song et al. [S10] SVG system demonstrated a high evaporation enthalpy of 2410 kJ/kg which is 1.7 and 1.9 times greater than PVA/1D-MnO_2(10%) and PVA/3D-MnO_2(10%) respectively.

The obtained PVA/MnO_2 hydrogel was then used for desalination application using sea water sampling at Sydney coast (Sydney Darling Harbor: 33.8749° S, 151.2009° E). The hydrogel was exposed to sunlight for 1 h and the evaporation rate was recorded. After the hydrogel was cooled down to room temperature, the evaporation testing was repeated. As shown in Fig. 7a, PVA/1D-MnO_2(10%) managed to produce freshwater with an average of 2.8 kg/(m^2·h) evaporation rate in 13-cycle testing. Of particular note, we did not observe severe salt accumulation on the surface of the hydrogel, thus high evaporation rate was maintained in the desalination application. These results indicate high durability, high performance stability and high salt resistance of the PVA/MnO_2 hydrogel SVG system. The water vapor was then condensed and collected. The ions concentrations in the produced water were also

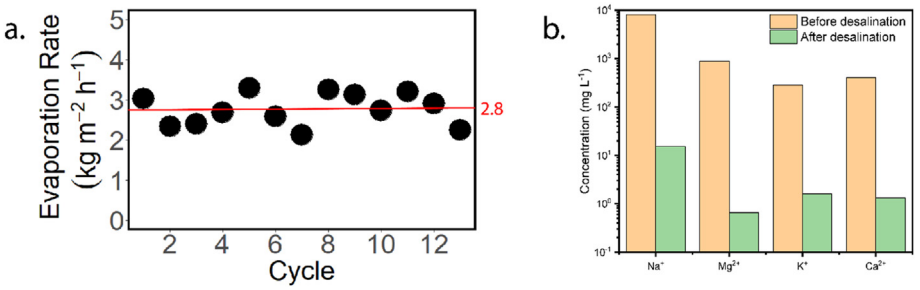

Fig. 7. (a) Evaporation performance stability and (b) the ICP-MS results of the PVA/MnO_2 hydrogel SVG in desalination application.

determined using ICP-MS. As shown in Fig. 7b, over 99% of salts (Na^+, Mg^{2+}, K^+, and Ca^{2+}) has been removed and the produced water far exceeds the WHO drinking water standard [50–52].

4. Conclusion

A novel 1D metal oxide semiconductor was synthesized and incorporated into the PVA matrix to form a hydrogel-based SVG system. The 1D MnO_2 displayed broad absorption range, high surface hydrophilicity and high light-to-heat conversion efficiency. The resultant hydrogel SVG system managed to produce a high-water evaporation rate of 2.8 kg/(m^2·h) in both control and sea water desalination experiments with a very high energy conversion efficiency. The hydrogel SVG also displayed high durability and high salt resistance, achieving a stable evaporation performance in a long-term testing.

Declaration of competing interest

The authors declare that they have no known competing financial interests or personal relationships that could have appeared to influence the work reported in this paper.

Acknowledgements

C.O. acknowledges support of the Australian Government Research Training Program Scholarship from the University of Technology Sydney. Q.F. acknowledges the Australian Research Council under the Future Fellowship (FT180100312).

Appendix A. Supplementary data

Supplementary data to this article can be found online at https://doi.org/10.1016/j.efmat.2022.08.001.

References

[1] UNESCO WWAP, The United Nations World Water Development Report 2020: Water and Climate Change WWDR 2020, UNESCO, 2020.
[2] A. Boretti, L. Rosa, Reassessing the projections of the world water development report, npj Clean Water 2 (2019) 1–6.
[3] C.M. Flores-Cayuela, R. González-Perea, E. Camacho-Poyato, P. Montesinos, Verifiable water use inventory using ICTs in industrial agriculture, in: S.S. Muthu (Ed.), Water Footprint Assessment and Case Studies, Springer Singapore, Singapore, 2021, pp. 1–34.
[4] A. Godoy-Faúndez, D. Rivera, D. Aitken, M. Herrera, L. El Youssfi, Circular economy in a water-energy-food security nexus associate to an SDGs framework: understanding complexities, in: L. Liu, S. Ramakrishna (Eds.), An Introduction to Circular Economy, Springer Singapore, Singapore, 2020, pp. 219–239.
[5] H. Müller Schmied, D. Cáceres, S. Eisner, M. Flörke, C. Herbert, C. Niemann, T Asali Peiris, E. Popat, F. Theodor Portmann, R. Reinecke, M. Schumacher, S. Shadkam, C.E. Telteu1, T. Trautmann, P. Döll, The global water resources and use model WaterGAP v2.2d: model description and evaluation, Geosci. Model Dev. (GMD) 14 (2021) 1037–1079.
[6] Y. Wada, M. Flörke, N. Hanasaki, S. Eisner, G. Fischer, S. Tramberend, Y. Satoh, M.T.H. van Vliet, P. Yillia, C. Ringler, P. Burek, D. Wiberg, Modeling global water use for the 21st century: the water futures and solutions (WFaS) initiative and its approaches, Geosci. Model Dev. (GMD) 9 (2016) 175–222.
[7] L. Linkola, C.J. Andrews, T. Schuetze, An agent based model of household water use, Water 5 (2013) 1082–1100.
[8] L. Goette, C. Leong, N. Qian, Motivating household water conservation: a field experiment in Singapore, PLoS One 14 (2019), e0211891.
[9] M.J. Hackett, N. Gray, Carbon dioxide emission savings potential of household water use reduction in the UK, J. Sustain. Dev. 2 (2009) 36.
[10] S. Peter, Troubled Waters Confronting the Water Crisis in Australia's Cities, ANU Press, Canberra, 2008.
[11] H.H. Hasan, S.F. M Razali, N.H. M Razali, Does the household save water? evidence from behavioral analysis, Sustainability 13 (2021) 641.
[12] H.H.G. Savenije, Water scarcity indicators; the deception of the numbers, Phys. Chem. Earth - Part B Hydrol., Oceans Atmos. 25 (2000) 199–204.
[13] G. Mao, H. Hu, X. Liu, J. Crittenden, N. Huang, A bibliometric analysis of industrial wastewater treatments from 1998 to 2019, Environ. Pollut. 275 (2021), 115785.
[14] W.-K. Ho, J.C.-F. Law, T. Zhang, K.S.-Y. Leung, Effects of weathering on the sorption behaviour and toxicity of polystyrene microplastics in multi-solute systems, Water Res. 187 (2020), 116419.
[15] J. Duan, N. Bolan, Y. Li, S. Ding, T. Atugoda, M. Vithanage, B. Sarkar, D.C.W. Tsang, M.B. Kirkham, Weathering of microplastics and interaction with other coexisting constituents in terrestrial and aquatic environments, Water Res. 196 (2021) 117011.
[16] A.H. M Saadat, M.S. Islam, P. Fahmida, A. Sultana, Desalination technologies for developing countries: a review, J. Sci. Res. 10 (2018) 77–97.
[17] V.G. Gude, N. Nirmalakhandan, S. Deng, Renewable and sustainable approaches for desalination, Renew. Sustain. Energy Rev. 14 (2010) 2641–2654.
[18] V.G. Gude, Desalination and sustainability – an appraisal and current perspective, Water Res. 89 (2016) 87–106.
[19] Y. Tu, R. Wang, Y. Zhang, J. Wang, Progress and expectation of atmospheric water harvesting, Joule 2 (2018) 1452–1475.
[20] N. Ghaffour, T.M. Missimer, G.L. Amy, Technical review and evaluation of the economics of water desalination: current and future challenges for better water supply sustainability, Desalination 309 (2013) 197–207.
[21] X. Zhang, T. Li, W. Liao, D. Chen, Z. Deng, X. Liu, B. Shang, A water supply tunable bilayer evaporator for high-quality solar vapor generation, Nanoscale 14 (2022) 7913–7918.
[22] X. Zhou, F. Zhao, Y. Guo, Y. Zhang, G. Yu, A hydrogel-based antifouling solar evaporator for highly efficient water desalination, Energy Environ. Sci. 11 (2018) 1985–1992.
[23] A.S. Alketbi, A. Raza, M. Sajjad, H. Li, F. AlMarzooqi, T. Zhang, Direct solar vapor generation with micro-3D printed hydrogel device, EcoMat 4 (2022), e12157.
[24] F. Zhao, Y. Guo, X. Zhou, W. Shi, G. Yu, Materials for solar-powered water evaporation, Nat. Rev. Mater. 5 (2020) 388–401.
[25] Y. Liu, H. Liu, J. Xiong, A. Li, R. Wang, L. Wang, X. Qin, J. Yu, Bioinspired design of electrospun nanofiber based aerogel for efficient and cost-effective solar vapor generation, Chem. Eng. J. 427 (2022), 131539.
[26] S. Li, X. Yang, Y. He, Y. Wang, D. Liao, Y. Chen, H. Xie, H. Liu, L. Zhou, Hierarchical porous aero-cryogels for wind energy enhanced solar vapor generation, Cellulose 29 (2022) 953–966.
[27] P. Wang, Emerging investigator series: the rise of nano-enabled photothermal materials for water evaporation and clean water production by sunlight, Environ. Sci.: Nano 5 (2018) 1078–1089.
[28] F. Yu, Z. Chen, Z. Guo, M.S. Irshad, L. Yu, J. Qian, T. Mei, X. Wang, Molybdenum carbide/carbon-based chitosan hydrogel as an effective solar water evaporation accelerator, ACS Sustainable Chem. Eng. 8 (2020) 7139–7149.
[29] J. Fang, Q. Liu, W. Zhang, J. Gu, Y. Su, H. Su, H. Su, C. Guo, D. Zhang, Ag/diatomite for highly efficient solar vapor generation under one-sun irradiation, J. Mater. Chem. A. 5 (2017) 17817–17821.
[30] S. Liu, C. Huang, Q. Huang, F. Wang, C. Guo, A new carbon-black/cellulose-sponge system with water supplied by injection for enhancing solar vapor generation, J. Mater. Chem. A. 7 (2019) 17954–17965.
[31] Y. Sui, D. Hao, Y. Guo, Z. Cai, B. Xu, A flowerlike sponge coated with carbon black nanoparticles for enhanced solar vapor generation, J. Mater. Sci. 55 (2020) 298–308.
[32] Q. Huang, C. Huang, S. Liu, F. Wang, C. Guo, Solar vapor generation optimization of a carbon-black/wood-flour system with strength enhanced by polystyrene, Int. J. Energy Res. 44 (2020) 3687–3696.
[33] A. Guo, X. Ming, Y. Fu, G. Wang, X. Wang, Fiber-based, double-sided, reduced graphene oxide films for efficient solar vapor generation, ACS Appl. Mater. Interfaces 9 (2017) 29958–29964.
[34] F. Wang, D. Wei, Y. Li, T. Chen, P. Mu, H. Sun, Z. Zhu, W. Liang, A. Li, Chitosan/reduced graphene oxide-modified spacer fabric as a salt-resistant solar absorber for efficient solar steam generation, J. Mater. Chem. A. 7 (2019) 18311–18317.
[35] G. Hu, Y. Cao, M. Huang, Q. Wu, K. Zhang, X. Lai, J. Tu, C. Tian, J. Liu, W. Huang, L. Ding, Salt-resistant carbon nanotubes/polyvinyl alcohol hybrid gels with tunable water transport for high-efficiency and long-term solar steam generation, Energy Technol. 8 (2020), 1900721.
[36] J. Wang, Y. Dang, A.G. Meguerdichian, S. Dissanayake, T. Kankanam-Kapuge, S. Bamonte, Z.M. Tobin, L.A. Achola, S.L. Suib, Water harvesting from the atmosphere in arid areas with manganese dioxide, Environ. Sci. Technol. Lett. 7 (2020) 48–53.
[37] Y. Wang, C. Wang, X. Song, S.K. Megarajan, H. Jiang, A facile nanocomposite strategy to fabricate a rGO–MWCNT photothermal layer for efficient water evaporation, J. Mater. Chem. A. 6 (2018) 963–971.
[38] H. Sun, Y. Li, J. Li, Z. Zhu, W. Zhang, W. Liang, C. Ma, A. Li, Facile preparation of a carbon-based hybrid film for efficient solar-driven interfacial water evaporation, ACS Appl. Mater. Interfaces 13 (2021) 33427–33436.
[39] F. Zhao, X. Zhou, Y. Shi, X. Qian, M. Alexander, X. Zhao, S. Mendez, R. Yang, L. Qu, G. Yu, Highly efficient solar vapour generation via hierarchically nanostructured gels, Nat. Nanotechnol. 13 (2018) 489–495.
[40] D. Jaganyi, M. Altaf, I. Wekesa, Synthesis and characterization of whisker-shaped MnO_2 nanostructure at room temperature, Appl. Nanosci. 3 (2013) 329–333.
[41] J.M.d.O. Cremonezzi, D.Y. Tiba, S.H. Domingues, Fast synthesis of δ-MnO_2 for a high-performance supercapacitor electrode, SN Appl. Sci. 2 (2020) 1689.
[42] H.S. Mansur, C.M. Sadahira, A.N. Souza, A.A.P. Mansur, FTIR spectroscopy characterization of poly (vinyl alcohol) hydrogel with different hydrolysis degree and chemically crosslinked with glutaraldehyde, Mater. Sci. Eng. C 28 (2008) 539–548.
[43] Y. Guo, J. Bae, Z. Fang, P. Li, F. Zhao, G. Yu, Hydrogels and hydrogel-derived materials for energy and water sustainability, Chem. Rev. 120 (2020) 7642–7707.
[44] S. Agnihotri, S. Mukherji, S. Mukherji, Antimicrobial chitosan–PVA hydrogel as a nanoreactor and immobilizing matrix for silver nanoparticles, Appl. Nanosci. 2 (2012) 179–188.

[45] Y. Murali Mohan, K. Lee, T. Premkumar, K.E. Geckeler, Hydrogel networks as nanoreactors: a novel approach to silver nanoparticles for antibacterial applications, Polymer 48 (2007) 158–164.
[46] P. Nikpour, H. Salimi-Kenari, F. Fahimipour, S.M. Rabiee, M. Imani, E. Dashtimoghadam, L. Tayebibf, Dextran hydrogels incorporated with bioactive glass-ceramic: nanocomposite scaffolds for bone tissue engineering, Carbohydr. Polym. 190 (2018) 281–294.
[47] J. Zhou, Y. Gu, P. Liu, P. Wang, L. Miao, J. Liu, A. Wei, X. Mu, Ji Li, J. Zhu, Development and evolution of the system structure for highly efficient solar steam generation from zero to three dimensions, Adv. Funct. Mater. 29 (2019), 1903255.
[48] H. Lim, M. Kim, J. Yoo, D. Lee, M. Lee, B. Na, S.K. Kim, Environmentally safe and renewable solar vapor generation device based on prussian blue nanoparticles immobilized on cellulose nanofibers, Desalination 524 (2022), 115477.
[49] X. Li, J. Li, J. Lu, N. Xu, C. Chen, X. Min, B. Zhu, H. Li, L. Zhou, S. Zhu, T. Zhang, J. Zhu, Enhancement of interfacial solar vapor generation by environmental energy, Joule 2 (2018) 1331–1338.
[50] O. World Health, Potassium in Drinking-Water : Background Document for Development of WHO Guidelines for Drinking-Water Quality, World Health Organization, Geneva, 2009.
[51] O. World Health, Calcium and Magnesium in Drinking Water : Public Health Significance, World Health Organization, Geneva, 2009.
[52] O. World Health, Guidelines for Drinking-Water Quality, fourth ed. ed, World Health Organization, Geneva, 2011.